Highly Sensitive Glucose Sensors Based on Gated Graphene Microwave Waveguides

*Patrik Gubeljak Tianhui Xu Jan Wlodarczyk William Eustace Oliver J. Burton Stephan Hofmann George G. Malliaras Antonio Lombardo**

P. Gubeljak
Department of Engineering, University of Cambridge, 9 JJ Thomson Avenue, Cambridge CB3 0FA, UK

T. Xu
Department of Electronic and Electrical Engineering, University College London, Gower Street, London WC1E 7JE
Department of Engineering, University of Cambridge, 9 JJ Thomson Avenue, Cambridge CB3 0FA, UK

W. Eustace, O.J. Burton, S. Hofmann, G. G. Malliaras
Department of Engineering, University of Cambridge, 9 JJ Thomson Avenue, Cambridge CB3 0FA, UK

J. Wlodarczyk
Department of Electronic and Electrical Engineering, University College London, Gower Street, London, United Kingdom, WC1E 7JE

A. Lombardo
London Centre for Nanotechnology, University College London, 17-19 Gordon Street, London, United Kingdom, WC1H 0AH
Department of Electronic and Electrical Engineering, University College London, Gower Street, London, United Kingdom, WC1E 7JE
Department of Engineering, University of Cambridge, 9 JJ Thomson Avenue, Cambridge CB3 0FA, UK

Email Address: a.lombardo@ucl.ac.uk

Keywords: *Microwaves, Sensors, Graphene, Microfludics, Machine Learning, Glucose Sensing*

A novel approach is demonstrated to identify glucose concentration in aqueous solutions based on the combined effect of its frequency-dependent interaction with microwaves propagating in graphene channels and the modification of graphene RF conductivity caused by physisorbed molecules. This approach combines broadband microwave sensing and chemical field effect transistor sensing in a single device, leading to information-rich, multidimensional datasets in the form of scattering parameters. A sensitivity of 7.30 dB/(mg/L) is achieved, significantly higher than metallic state-of-the-art RF sensors. Different machine learning methods are applied to the raw, multidimensional datasets to infer concentrations of the analyte, without the need for parasitic effect removals *via* de-embedding or circuit modeling, and a classification accuracy of 100% is achieved for aqueous glucose solutions with a concentration variation of $0.09\,\mathrm{mg\,L^{-1}}$.

1 Introduction

Microwaves interact with matter causing frequency-dependent reorientation of molecular dipoles and motion of ions and electrons [1]. Different molecules exhibit specific dipolar momenta, size, and composition, leading to different dielectric properties. Dielectric spectroscopy consists of the analysis of the real and imaginary parts of the permittivity as a function of frequency, which allows the identification of molecules *via* their "dielectric signature". Due to the diverse dielectric permittivity of biological molecules compared to water, microwave biosensors can detect multiple features of biological substances in solutions. For example, carbohydrates and amino acids can be differentiated by the shift of the real and imaginary parts of their permittivity with respect to de-ionized water at 20 GHz [2]. In liquids, the dielectric signature mainly depends on the properties of constituent molecules, including effective volume, dipole moment, *etc.* However, in solutions or dispersions, the permittivity is influenced not only by the individual properties of the component molecules but also by the interaction between the molecules of the solvent and the solute, which can change the polarisability and relaxation time of the dipoles [3]. Microwaves probe rotation and diffusion of polar molecules and the associated dielectric relaxation processes [4], which distinguishes microwave sensing from direct current (DC), low frequency and optical

methods. The relaxation behaviour of polar molecules such as water can be described by the Debye model, and the relative permittivity ε_r, is given by [5] :

$$\varepsilon_r = \varepsilon_\infty + \frac{(\varepsilon_s - \varepsilon_\infty)}{1 + (j\omega\tau)} - \frac{j\sigma}{\omega\epsilon_0} \tag{1}$$

where ε_∞ is the high-frequency permittivity, ε_s is the low-frequency permittivity, ω is the angular frequency, τ is the relaxation time, and σ is the ionic conductivity.
In solution and dispersion, especially those including biological materials, the overall relaxation depends on multiple processes. The Debye model has to be modified by introducing an empirical value α in the so-called Cole-Cole model [6]:

$$\varepsilon_r = \varepsilon_\infty + \frac{(\varepsilon_s - \varepsilon_\infty)}{1 + (j\omega\tau)^\alpha} - \frac{j\sigma}{\omega\epsilon_0} \tag{2}$$

Microwave sensing is typically achieved by placing the solution/dispersion to be tested in close proximity to a circuit where waves are propagating and measuring its dielectric properties *via* its effect on the wave propagation [6]. Microwave sensors usually consist of planar metallic structures (such as coplanar waveguides and microstrips), where the sensing is entirely due to the interaction of solution/dispersion with the electric field of the propagating waves. All of these structures rely on the electric and magnetic fields partially extending outside of the guiding structure, the so-called fringing field. Materials and molecules placed onto the structures interact with the fringing field, modifying the wave propagation within them and therefore the relative permittivity of the sensor. Metallic microwave sensors have been successfully used for studying brain tissue, glucose concentration [7, 8], cancer cells [9], cell membranes, and single (alive) cell analysis [2, 10, 11]. Microwave sensors are intrinsically label-free; however, they can also be combined with biomarkers to increase their specificity. They provide real-time reading, consume little power ($\sim mW$), have a very small form factor, and can be integrated with off-the-shelf radio frequency (RF) circuitry used for wireless and mobile communication [12]. A particular benefit of this approach is that microwaves are not affected by Debye screening due to the ions in the solution, which limits sensitivity at DC and low frequency. This allows the detection of molecules even in highly ionic concentration media, such as those encountered for biosensing under physiological conditions [13, 11].
Several types of structures have been used for this purpose, ranging from reflectometers, resonators, interferometers, and coplanar waveguides, each with specific advantages and trade-offs [6]. Reflectometers are simple to design and set up, but the signal does not propagate far into the material under test, and the sensitivity is typically small. Resonators offer much higher sensitivity, however, they are more complex and work only at narrow frequency ranges, limiting their "fingerprinting" capability. Interferometers combine high sensitivity and broadband operation but at the cost of increased circuit complexity. Coplanar waveguide sensors, are inherently broadband and simpler to design and analyze compared to other structures and can be easily integrated with other circuitry. Coplanar waveguide sensors typically have a relatively low resolution for glucose measurements, and most studies focus only on high concentrations, well above physiologically-relevant values. For example, the miniaturized sensor proposed by Ref. [14], considered aqueous solutions with a glucose concentration ranging between 0.3 and 80 g/L achieving a resolution of 0.4 g/L, only marginally smaller than the normal blood glucose concentration range in a healthy individual ($0.7 - 1$ g/L) and significantly larger than the glucose concentration in sweat ($10 - 36$ mg/L). However, the sensitivity of RF sensors can be significantly improved by replacing part of the metallic structure with graphene, which provides an additional sensing mechanism due to the modification of its RF conductivity further by chemical doping, generating information-rich, multidimensional datasets [15, 16].
Graphene is an atomically-thin material consisting of a single layer of carbon atoms tightly arranged in a hexagonal lattice. Since the groundbreaking experiment that investigated its electronic properties [17], much attention has been devoted to using it in sensors due to its "ultimate" surface-to-volume ratio, in combination with good conductivity, ambipolar field effect, biocompatibility, and ease of functionalization. Due to its thickness, graphene's electronic properties are strongly modified by the environment and

therefore the variety of chemical species that interact with it. These range from gases, as in the case of the first graphene chemical sensor [18], to different (bio)chemical species such as DNA, cholesterol, enzymes, proteins, even viruses and living cells [19]. Graphene and its chemical derivatives are also promising for wearable sensors [20].

Graphene is now produced on a large industrial scale and has already been used in some commercial electronic products [21]. Pilot production lines have recently been established and graphene-covered wafers are commercially available [22], enabling wide-scale adoptions of graphene device technologies. Graphene biosensors are typically chemical field effect transistors (ChemFETs), where the transistor channel is exposed to the analyte. The addition of the analyte then changes the charge density, *i.e.* chemically dope the transistor channel. For (bio-)chemical material sensing, these transistors have been integrated into microfluidic setups used to deliver the analyte solution with a global, electrolytic gate electrode. Initially, the sensing itself was accomplished amperometrically by tracking the changes in the source-drain current at fixed DC operating points while changing the composition or concentration of the analyte solution [23]. More recent work has built on that by comparing the $I_{DS} - V_{GS}$ transfer curves of the transistors, where the changes in doping brought on by the analyte shift the point of minimum conductivity of the ChemFET, *i.e.* the charge neutrality point (CNP) [24]. This is also the typical mechanism used for glucose sensing. Often graphene glucose sensors rely on heterostructures or surface functionalization [25, 26]. Graphene sensors without surface functionalization have been successfully used to detect small concentrations of glucose, down to 0.5 mM (9 mg/dL), as the intermolecular van der Waals forces between glucose and graphene are several times stronger than those between graphene and water [27, 28], and hence glucose displaces the water molecules on the surface of graphene.

The AC conductivity of graphene can be described by the Kubo formalism, as shown in Equation 3 below [29].

$$\sigma_{\text{intra}}\left(\omega, E_F, \tau, T\right) = \frac{\mathrm{i}e^2 k_B T}{\pi\hbar^2\left(\omega + i\tau^{-1}\right)}\left[\frac{E_F}{k_B T} + 2\ln\left(1 + \mathrm{e}^{-\frac{E_F}{k_B T}}\right)\right] \tag{3}$$

where: $\omega = 2\pi f$ is the angular frequency, E_F is the Fermi energy, τ is the scattering time (assumed to be independent of energy), T is the temperature expressed in Kelvin, $e = 1.6 \cdot 10^{-19}$ C is the electron charge, $\hbar = \frac{h}{2\pi}$ is the reduced Planck's constant, and $k_B = 1.38 \cdot 10^{-23}\ \frac{\text{J}}{\text{K}}$ is Boltzmann's constant. The equation suggests that if the angular frequency is much smaller than the scattering rate ($\omega \ll 2\pi/\tau$), the graphene AC conductivity is largely frequency-independent and equal to DC conductivity. Based on experimental measurements of $\tau \approx 0.05 - 1$ ps [30, 31, 32, 33], this approximation is valid for frequencies up to $\approx$ 500 GHz [29]. Therefore, when graphene is integrated into microwave sensors, variations of waveguide parameters can be directly attributed to the solution/dispersion under test. As graphene's conductivity (AC and DC) is significantly modified by chemical doping, which changes E_F in Eq. 3, resulting from molecule absorption when in contact with analytes, this strongly affects the propagation of electromagnetic waves and provides a second concurrent sensing mechanism for microwave sensors.

In a microwave sensor, the interaction of electromagnetic waves with analytes is captured by the so-called scattering (S) parameters, measured *via* a vector network analyzer (VNA). S-parameters define the ratio between a known stimulus (*i.e.* waves of well-defined amplitude, frequency, and phase) and the corresponding response, measured at the device ports. However, S-parameters are not a direct measurement of material properties, and significant data analysis and fitting against models are required to extract the properties of analytes from S-parameters. Methods such as multiline [34], Nicholson-Ross-Weir (NRW) [35] or ABCD parameters [36] have to be applied to identify the relative permittivity of the sensor, which, in turn, must account for the sensor geometry and the permittivity of the material under test, requiring further modeling such as fitting with an RLCG circuit [37].

Machine learning (ML) and deep learning are particularly effective approaches to identify information from systems -like microwave circuits- whose output is determined by different contributions that are not easy to decouple [38]. Without experimental post-processing and further modeling, ML can distinguish signals from noise and identify chemical information as predictions from simulation data or experimental data based on a decision system, omitting measurement errors, approximations, and physical

model assumptions, and can therefore potentially lead to a faster and more accurate solution for sensing. Also, ML can be advantageous over conventional data analysis methods in terms of learning and extracting knowledge from multi-variety data and obtaining nonlinear dependencies between complex signals and chemical properties [39]. These properties highlight emerging efforts to couple ML with biosensing systems to improve the efficiency and accuracy of real sample measurements. For example, Artificial Neural Networks (ANNs) have been applied to identify the diffraction pattern of single molecules from noisy images obtained *via* a standard microscope [40], and Convolutional Neural Networks (CNNs) have been used for label-free flow cytometry, achieving cell sorting with decision times in milliseconds [41]. CNNs have also been used for the identification of cancer cells *via* their analysis of spectra generated by surface-enhanced Raman spectroscopy [42]. ML has also demonstrated high potential in near-infrared spectroscopy for blood glucose level detection [43]. In the context of microwave sensing, successful material classification and identification were achieved with ML using a complementary split ring resonator (CSRR) [44] and a broadband frequency comb receiver [45], while material permittivity measurement by ML has been demonstrated using open-ended coaxial probes [46]. By using a sufficiently large amount of sensing data with characteristic features, machine learning is expected to be capable of differentiating specific signatures of different analytes for prediction and classification without additional functionalization processes for sensors [47].

The determination of the dielectric properties of glucose solutions with conventional data processing methods [48, 49] has been studied in many works for the development of non-invasive blood glucose sensing devices. Ref. [50] achieved the measurement of the permittivity of glucose solutions and several organic solvents with an open-ended coaxial probe using ANNs and CNNs. However, such an approach is not sensitive enough when the variation of glucose concentration is small [51], and there are components other than glucose that may affect the changes in the blood glucose dielectric permittivity [52]. Therefore, a direct link between measurements and glucose concentrations is normally preferable. [53] demonstrated the classification of different glucose concentrations at blood glucose physiological levels through microwave sensing using coaxial probes. In Ref. [54], several ML regression models were used on the reflection coefficient (S_{11}) from an electrically-small dipole sensor, and as a proof of concept, a direct prediction of the concentrations of aqueous glucose solutions was achieved. Recently, ML was applied to microwave sensors consisting of metallic resonators coupled with microfluidic channels to detect gluose at concentrations between 25 and 500 mg/dL [55].

Here, we demonstrate a novel glucose sensor consisting of a graphene channel embedded in a CPW structure and coupled to microfluidic channels. We expose the sensors to aqueous solutions of glucose at small concentrations, down to 9 μg/dL (one order of magnitude smaller than sweat glucose physiological levels), producing multidimensional datasets from complex S-parameters obtained with both DC gate voltage sweep and RF frequency sweep. Our approach combines broadband microwave sensing and chemical field effect transistor sensing in a single device and results in a sensitivity of 7.30 dB/(mg/L), higher than any microwave sensor reported to date. Moreover, we study the complex S-parameter datasets by common ML models, achieving classification of different glucose concentrations with 100% accuracy.

2 Results and Discussion

2.1 Design and Fabrication

Our sensor consists of a graphene FET channel embedded in a CPW, to which we mount a microfluidic channel, as shown in Figure 1.

The main part of the waveguide was designed according to the Mechanical Layout Rules provided by the microwave probe manufacturer [56], with a standard impedance of 50 Ω to match the measuring system and reduce insertion loss. The tapered narrow section in the center of the waveguide serves to increase the strength of the electric fields of the propagating waves and reduces the size of the graphene channel to a width of 12.75 μm. The design was optimized by simulations in the frequency domain using Dassault Systems Simulia CST Studio Suite. Details of the simulations and a comparison between

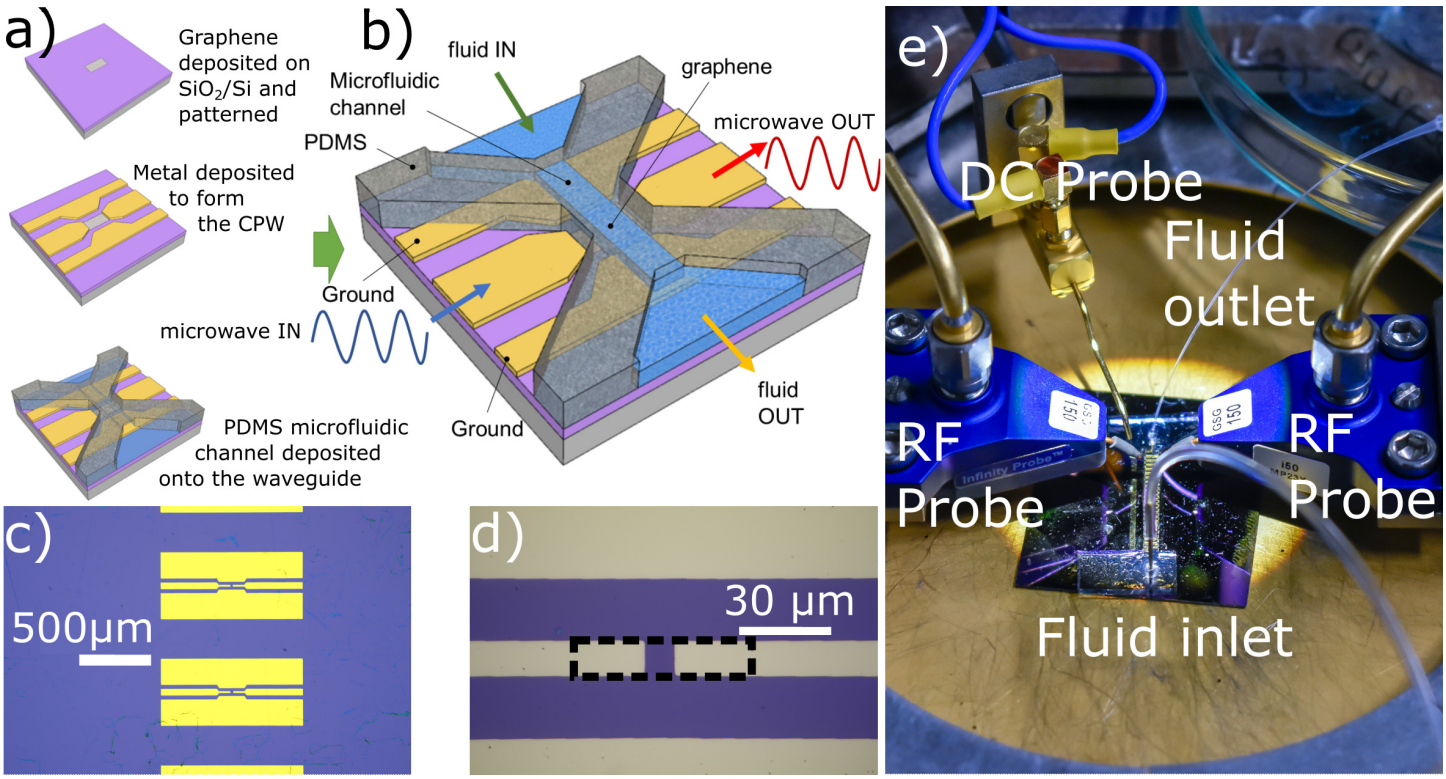

Figure 1: a) Fabrication steps of graphene microwave sensors b) Schematic of the sensor and measuring configuration. c) Representative devices part of an array before PDMS encapsulation. d) Close-up of a graphene channel embedded in the CPW (before fabrication of microfluidic channel). The dashed line indicates the graphene, including the overlap with metal contacts. e) Experimental setup consisting of RF and DC probes and microfluidic inlet and outlet mounted on a semi-automatic probe station.

simulated and experimental results for graphene and metallic waveguides are provided in the Supporting Information. The fabrication steps are shown in Figure 1a. CVD-grown graphene is deposited onto high-resistivity, oxidized (oxide thickness 295 nm SiO_2) Si substrates and integrated into coplanar waveguides by conventional microfabrication. PDMS microfluidic channels are fabricated using a SU8 epoxy resin mold and mounted perpendicularly to the coplanar waveguide, confining the interaction of the solution on the graphene channel. Microwaves launched at one port of the waveguide propagate through the graphene, thus interacting with the fluid moving in the channel both directly (*via* the fringing field) and indirectly (*via* changes of graphene conductivity due to chemical doping). Figure 1b shows the schematic of device operation. Arrays of graphene CPWs are fabricated on the same chip. In order to enable electrolytic gating, a planar gold counter-electrode is fabricated on the chip, with a surface area $\approx$ 2000 times larger than the area of the graphene channels. This maximizes the capacitance at the counter-electrode/liquid interface, making it negligible in the series capacitance resulting from counter electrode-liquid and liquid-graphene interfaces [57]. The counter-electrode also acts as an RF shield, reducing the effects of stray electromagnetic interference on the sensors. Figure 1c and Figure 1d show optical micrographs of fabricated devices (prior to deposition of the microfluidic channel), and Figure 1e shows the device mounted on a probe station setup and connected to testing instrumentation and microfluidic controller. The fabrication protocol is based on scalable methods, and the production of the sensor can be carried out entirely by a foundry for commercial manufacturing.

2.2 DC Measurement Analysis

We exposed the sensor to the analyte using an OB1 Mk3 microfluidic controller. We initially tested our sensors at DC, exposing them to nine (including DI water) different concentrations of glucose aqueous solution varying from 9 µg dL^{-1} to 5400 µg dL^{-1} at a flow of 1 µL min^{-1}. These concentrations are lower than physiological blood glucose levels [58] and comparable to glucose levels present in sweat. The pri-

mary objective was to extend the RF sensing principles to detect these ultra-low concentrations, which had been studied with state-of-the-art graphene DC sensors [59, 60]. The source-drain voltage (V_{ds}) was set to 100 mV, and the current was monitored as the fluid was flowing. A voltage sweep from 0 to 1 V was applied to the counter electrode, which acted as a global electrolytic gate. The voltage was applied in steps of 10 mV with a 1 s delay between steps to stabilize the current. The electrolyte gate sweeps were repeated 10 times to minimize the effect of hysteresis on the measurement. The resulting transfer curves are presented in Figure 2a below. From the initial position of the charge neutrality point (CNP), *i.e.* $V_g > 0$ V, the as-produced graphene device is p-doped. Exposing the devices to the glucose solution introduces n-doping, which counteracts the initial p-doping of graphene and causes the transfer curve and the CNP to shift to the left.
To measure the sensitivity of our sensor, we look at the value of the shift in the CNP of the 10^{th} transfer curve for each concentration compared to the transfer curve corresponding to exposure to de-ionized (DI) water, acquired during rinsing of the sensor before introducing the glucose solution. We take the shift of the CNP with respect to glucose concentration as a figure of merit for sensitivity, as shown in Figure 2b below.

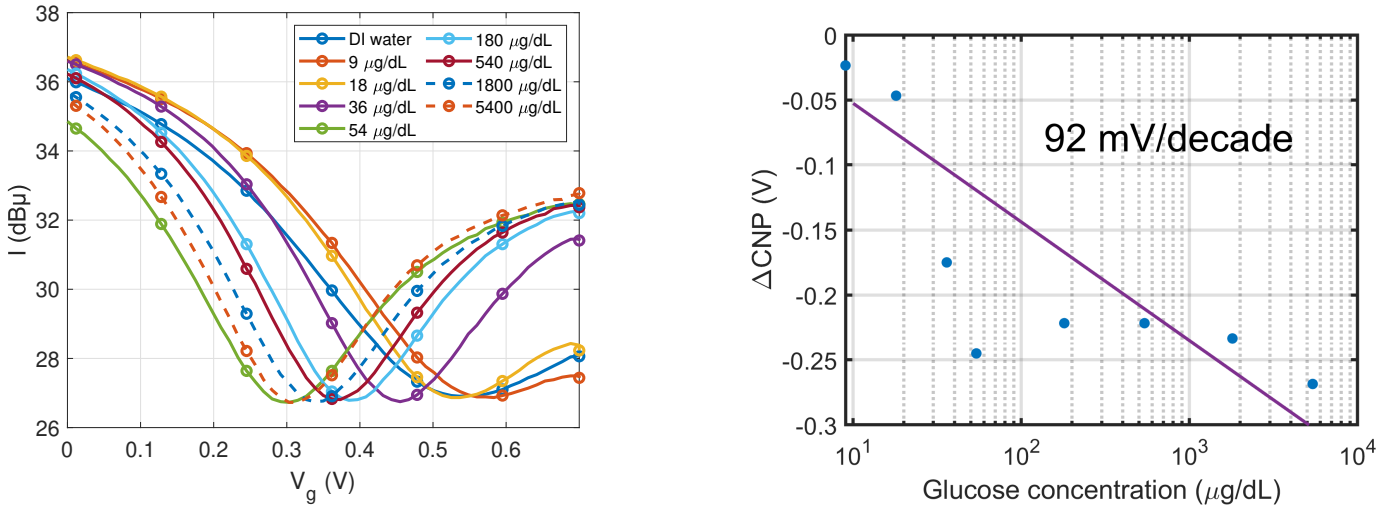

(a) I − V curves at 9 different glucose concentrations of one device.

(b) Changes of the charge neutrality point at different glucose concentrations.

Figure 2: Transistor transfer curves of an individual device. The ΔCNP data is used as the Figure of Merit for DC sensor performance.

From Figure 2b, we see that the shift in the CNP follows a clear and expected trend at low concentrations and appears to reach a saturation region. The sensitivity and limit of detection agree well with previously reported graphene glucose sensors [59], however without the need to modify the graphene with enzymes or Pt nanoparticles or small molecules. The linearized trend of the Δ CNP of the sensor also agrees with the previous reports in literature [59].
The apparent reversal of the trend at concentrations higher than 100 μg dL^{-1} can be attributed to concentration dependent changes in the electrical permittivity of the glucose solution [61]. The changes in permittivity affect the capacitance of the electrolytic gate, changing the amount of charge transferred for a given shift in the gate voltage, hence changing the doping induced in the graphene channel. The trend in the changing capacitance corresponds well to existing measurements of dielectric permittivity of glucose solutions in DI water. Such non-monotonic trends make calibration of purely DC sensors more difficult and/or limit their operating regimes, which we alleviate by pursuing RF techniques.

2.3 RF Measurement Analysis

RF measurements were performed using a VNA, connected to ground-signal-ground (GSG) probes through a bias network so we could apply both RF and DC signals through the same contact on the device. Prior

to RF measurements, the system was calibrated using an impedance standard substrate (ISS) using the multi Thru-Reflect-Line (mTRL) technique. For each glucose concentration, the RF measurements were performed directly after the DC measurements to minimize any drift. The frequency was swept from 50 MHz to 50 GHz, with RF power set to -12 dBm and the IF to 1 kHz to record the S-parameters. The measurements were repeated 10 times to generate datasets for ML model training.
The result of a 2-port RF measurement at a single frequency is a 2×2 complex-valued matrix of S-parameters at a given frequency. To record them over a wide frequency range, the measurement is repeated at every frequency of interest, resulting in a $2 \times 2 \times N$ three-dimensional array, where N is the number of frequency points. Since our device is passive and symmetric, $S_{11} \approx S_{22}$ and $S_{21} \approx S_{12}$. In standard RF methodology, the curves of an individual S-parameter (in our case, S_{11} and S_{21}) as a function of frequency would be compared to the predictions of a physical circuit model, whose properties would be fitted to match the measured data. Instead, we consider a surface of S-parameters, where the parameter surface is a function of frequency and gate voltage, as shown for S_{21} in Figure 3.

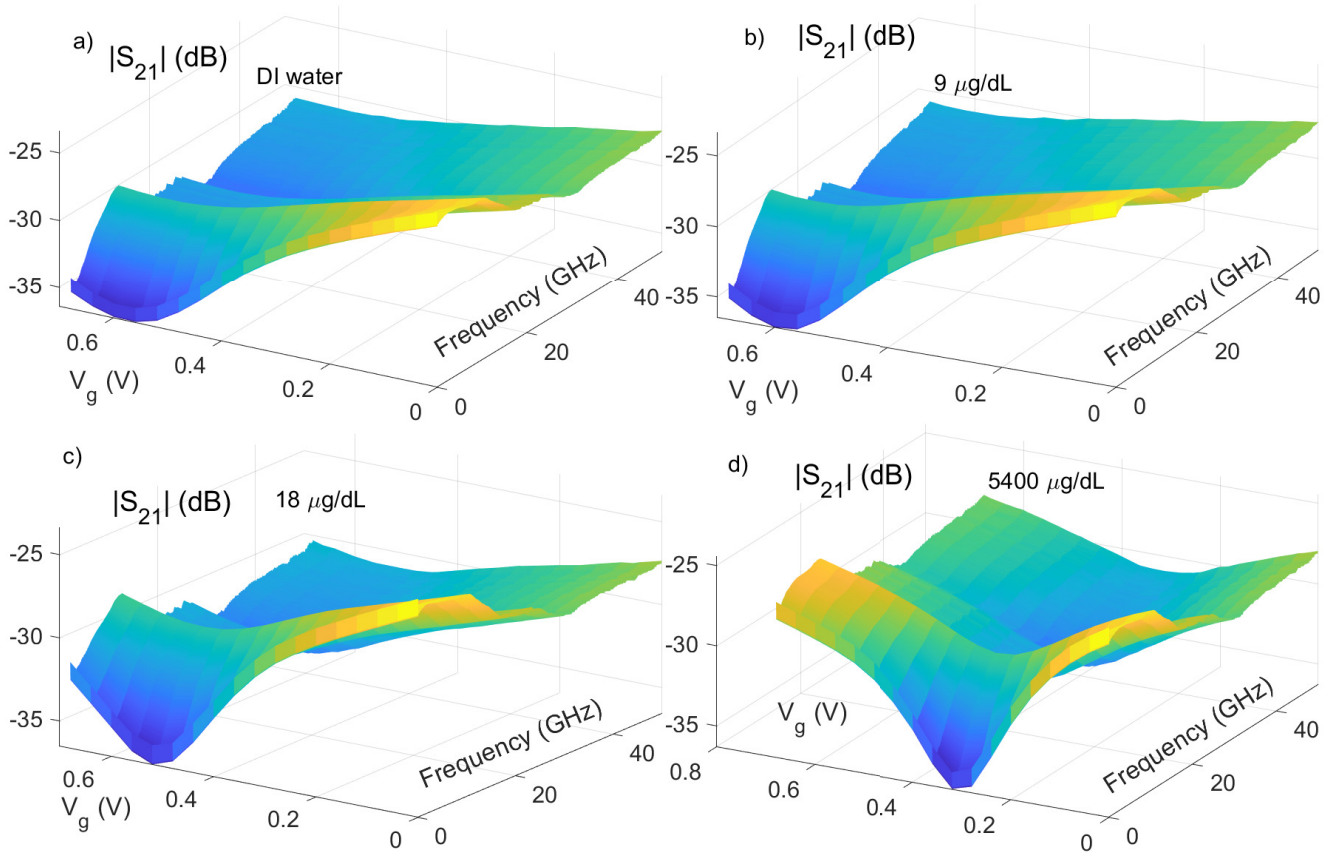

Figure 3: The magnitude of the the transmission parameters S_{21} for different glucose concentrations. a) The magnitude for DI water. b) Glucose concentration of 9 µg dL^{-1}, *i.e.* 0.5 µM. c) Glucose concentration of 18 µg dL^{-1}, *i.e.* 1 µM. d) Glucose concentration of 5400 µg dL^{-1}, *i.e.* 0.3 mM.

The S-parameter surface can be constructed as the chemical doping of the graphene channel modifies its RF conductivity, which would not be possible in metallic sensors. The differences between these surfaces need to be interpreted to obtain a figure which will encapsulate the change in the properties with the change in glucose concentrations and can thus be used as a figure of merit for the sensor. Initially, to more easily understand the RF behavior of the sensor as the concentration changes, we look at the differences in the S-parameters at a fixed frequency. Since we are also interested in simultaneous changes due to the gating, we plot the difference in the magnitude of S-parameters as a function of both the concentration and the applied DC gate bias, resulting in the surface shown in Figure 4 below. Essentially, we look at the difference in decibels (dB) at each specific gate voltage and concentration to obtain the surfaces. This allows for easy identification of the DC condition (*i.e.* V_g) at which the difference in S-

parameters is largest. We note this corresponds to the gate voltage at which also the DC sensitivity reaches a maximum, showing the strong link between the conductivity of graphene and resultant RF behavior.

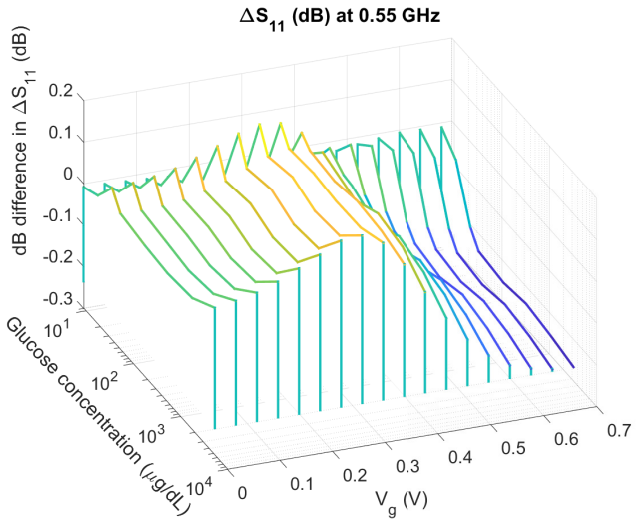

(a) Change in the magnitude of the reflection, *i.e.* S_{11}, parameter as a function of gate voltage and the glucose concentration.

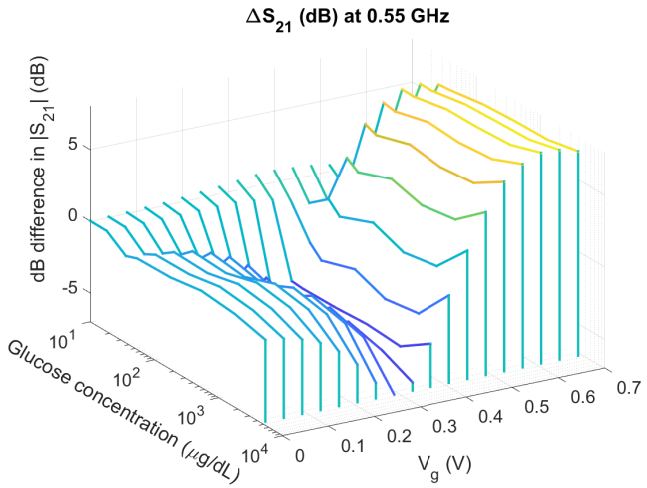

(b) Change in the magnitude of the transmission, *i.e.* S_{21}, parameter as a function of the gate voltage and the glucose concentration.

Figure 4: The curves of the change in the magnitude of S-parameters. The changes between the reflection and transmission have opposite signs, and it can be clear that the transmission parameter is much more strongly dependent on the concentration.

Returning back to Figure 3, the surface is not just shifted along the gate axis, but the features such as the minima/maxima and the gradient around them change with different concentrations. Rather than individual curves, *i.e.* slices at a given gate voltage along the frequency axis or slices at a given frequency along the gate voltage axis, being compared, the complete V_g-frequency surfaces are compared between different concentrations. This complex information motivated us to use ML methods to take into account multiple features presented on the surfaces.

2.4 DC vs. RF

A direct 1-to-1 comparison between the DC and RF measurements is not possible, as they have different dimensionalities. For each glucose concentration, DC measurements provide a two-dimensional set of data (current vs. gate voltage), whereas the RF measurement results provide a multidimensional dataset consisting of four complex numbers (or equivalently magnitude and phase) for each gate and frequency point. However, there are still some correlations that can be drawn between the DC and RF results. We compare the RF admittance with the DC conductance shown in Figure 5. We can see from Figure 5a that the relationship of the relative RF admittance Y_{21} amplitudes at different glucose concentrations is in general constant in the whole frequency range, while the DC curves have intersections at different gate voltages in Figure 5c due to the changes in graphene doping. However, the amplitude of the RF admittance and the DC conductance at different glucose concentrations are highly correlated at certain gate voltages, as shown in Figure 5b and d. The inset in a) shows a clearer admittance difference at different glucose concentrations, and the consistent sequential arrangement of the curves is useful for identifying glucose concentration variations in the whole frequency range. As stated in the Introduction, the conductivity of the material affects losses and hence the magnitude of the transmission parameters.

2.5 RF Sensitivity

We express the RF sensitivity in terms of Admittance parameters (Y-parameters) as follows:

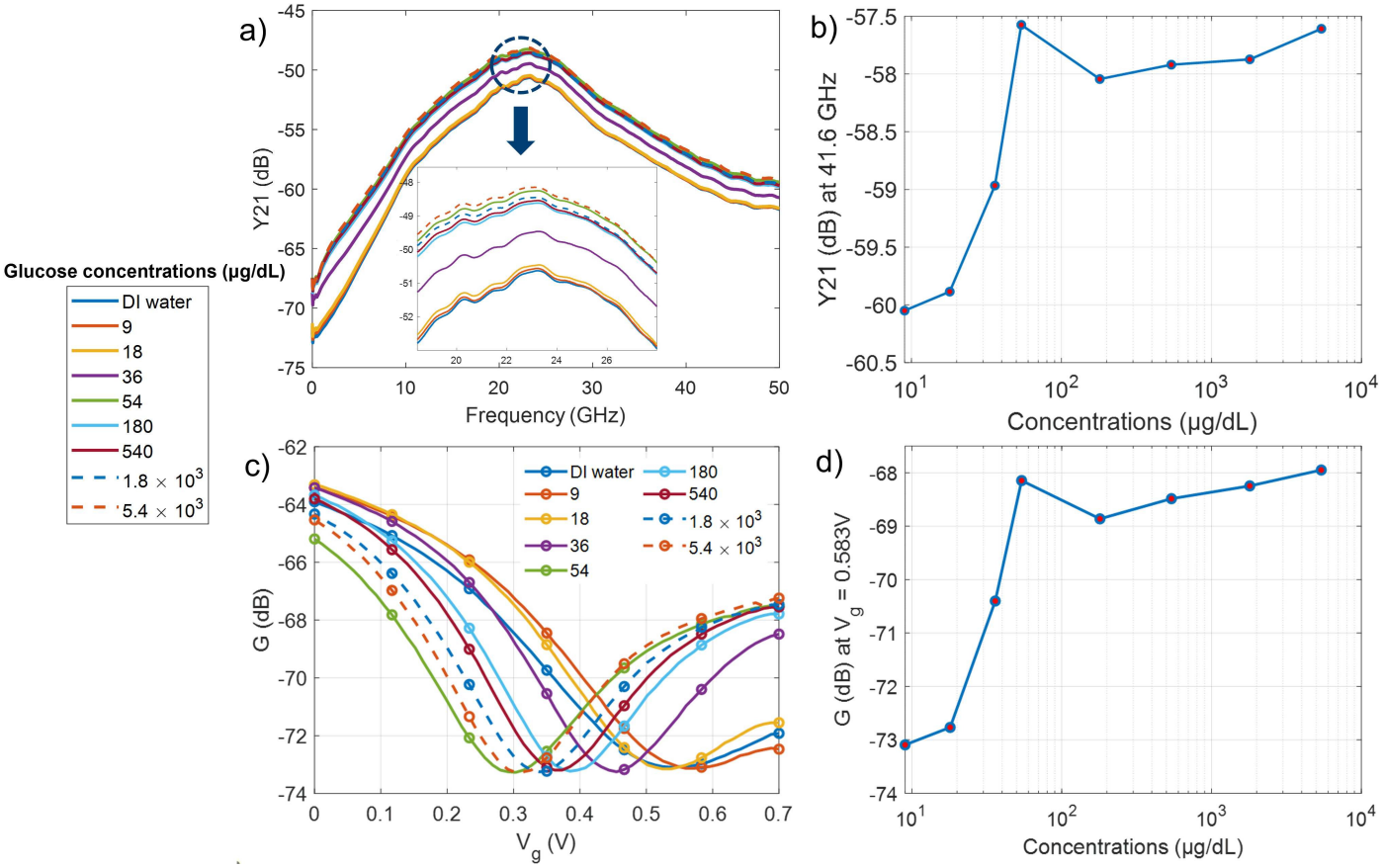

Figure 5: Comparison of RF admittance and DC conductance at nine different glucose concentrations. a) RF admittance at $V_g = 0.583V$ over the whole frequency range for the first nine low concentrations. b) RF admittance at 41.6 GHz for the first eight low concentrations (except DI water). c) DC conductance over the whole DC gate voltage sweep for the first nine low concentrations. d) DC conductance at $V_g = 0.583V$ for the first eight low concentrations (except DI water).

$$\frac{\Delta|Admittance|\ (at\ a\ certain\ frequency)}{\Delta[Glucose\ concentration]}\mathrm{dB/(mg/L)} \tag{4}$$

We investigated the sensitivity at concentrations between $9\,\mu g\,dL^{-1}$ to $5400\,\mu g\,dL^{-1}$. For comparison, this range is significantly larger than the concentration of glucose found in human sweat (approximately $1\,mg\,dL^{-1}$ to $4\,mg\,dL^{-1}$ [62]).

The sensitivity at each RF frequency point is obtained as the average of the sensitivities of the nine low concentrations calculated by Eq. 4. A high sensitivity demonstrates a high contrast between different glucose concentrations. Figure 6a shows the average sensitivity as function of frequency at $V_g = 0.28$V. The maximum sensitivity is 7.30 dB/(mg/L) at around 2.13 GHz. We note that the maximum sensitivity is achieved at frequencies very close to those used in wireless communication technology (*e.g.* 2.4 GHz is used in WiFi and Bluetooth networks), making our devices easy to integrate with consumer-level RF circuitry. Absolute sensitivities, calculated according to 4 are shown in Figure 6b. Sensitivities calculated with Y-parameters have similar values to those calculated with S-parameters.

Due to the differences in sensing mechanisms and in the considered glucose concentration ranges, for the sake of comparing our sensors with state-of-the-art sensors, we use the Relative Sensitivity (RS) concept proposed by [63]:

$$RS = \frac{\Delta SP}{SP_0 \times \Delta\alpha}\%/\%, \tag{5}$$

where α is the parameter to be measured, $\Delta\alpha$ is the relative change in α with respect to the lowest α involved in the operating range of the sensor, SP_0 is the operating value of the sensing parameter, and

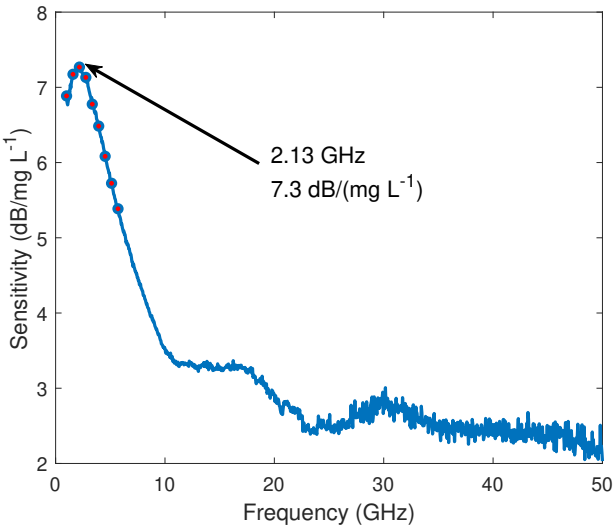

(a) Frequency sweep of RF sensitivities.

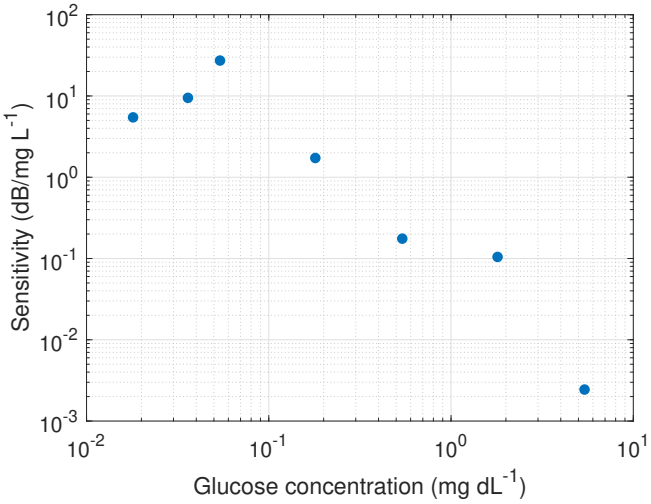

(b) RF sensitivities at different concentrations.

Figure 6: RF sensitivities.

ΔSP is the measured shift of SP. In our case, α is the glucose concentration, and SP is the Admittance parameter.

The RS for aqueous glucose sensing of the sensor in this work is 7.07 %/% at 2.13 GHz. A review of the performance of different metallic microwave planar resonant sensors for glucose sensing is summarized in Ref. [63]. The microwave-based sensor made from a bandstop filter by [14] reached a sensitivity of 7.6×10^{-6} dB/(mg/L) and a RS of 4.889 %/% by looking at the amplitude of S_{21} for glucose concentrations ranging from $0.3\,\mathrm{g\,L^{-1}}$ to $80\,\mathrm{g\,L^{-1}}$. The microstrip line (MLIN)-based glucose sensor (MSCS) proposed by [64] showed a good sensitivity of 0.52×10^{-4} dB/(mg/L) and a RS of 2.344 %/% using S_{11} amplitude at low concentrations ranging from 0-120 $\mathrm{mg\,dL^{-1}}$, and the sensor composed of two cells of circular split ring resonator in the recent work by [65] has a sensitivity of 0.42×10^{-4} dB/(mg/L) and a RS of 3.923 %/% based on S_{11} amplitude for a concentration range of 31.2-250 $\mathrm{mg\,dL^{-1}}$. With the incorporation of graphene, the broadband, non-functionalized sensor reported in this paper achieved a relative glucose sensitivity larger than any metallic state-of-the-art microwave sensor. In the SI, a comparison (both simulation and experimental) between graphene and metallic sensors of identical design and dimensions is reported.

2.6 Data Preprocessing for Machine Learning

It can be observed in Figure 7b, c, d and Supplementary Figure 5 that S-parameters at different glucose concentrations vary at different frequencies, while the variations are difficult to distinguish at small concentration differences; for example, the S_{21} amplitude curves overlap with each other at the first three concentrations in Figure 7b. Also, Figure 3 and Figure 7a indicate that the V_g - Frequency surface of the S_{21} amplitude at different glucose concentrations exhibit complex behaviors, which are challenging to analyze thoroughly with conventional analytical or statistical methods. Therefore, in order to achieve the accurate and fast classification of different glucose concentrations based on the high-dimensional measurement results, we use ML to analyze the rich chemical, physical, and mechanical information of analytes imprinted in the complicated signals produced by our device.

Multiple datasets with different feature compositions are constructed for ML model training. Dataset A is constructed with the concatenated four parts of S_{11} and S_{21} over the whole frequency range at the gate voltage of the charge neutrality point, specifically, $[Re(S_{11}) \quad Im(S_{11})]$ and $[Re(S_{21}) \quad Im(S_{21})]$. To reduce feature dimension, Principal Component Analysis (PCA) is utilized, and 6 principal components are constructed from all frequency points, with 99% variance explained. The final dataset has the dimension of 224×6; 224 is 28 concentrations times 8 repeated measurements, and 6 is the feature number

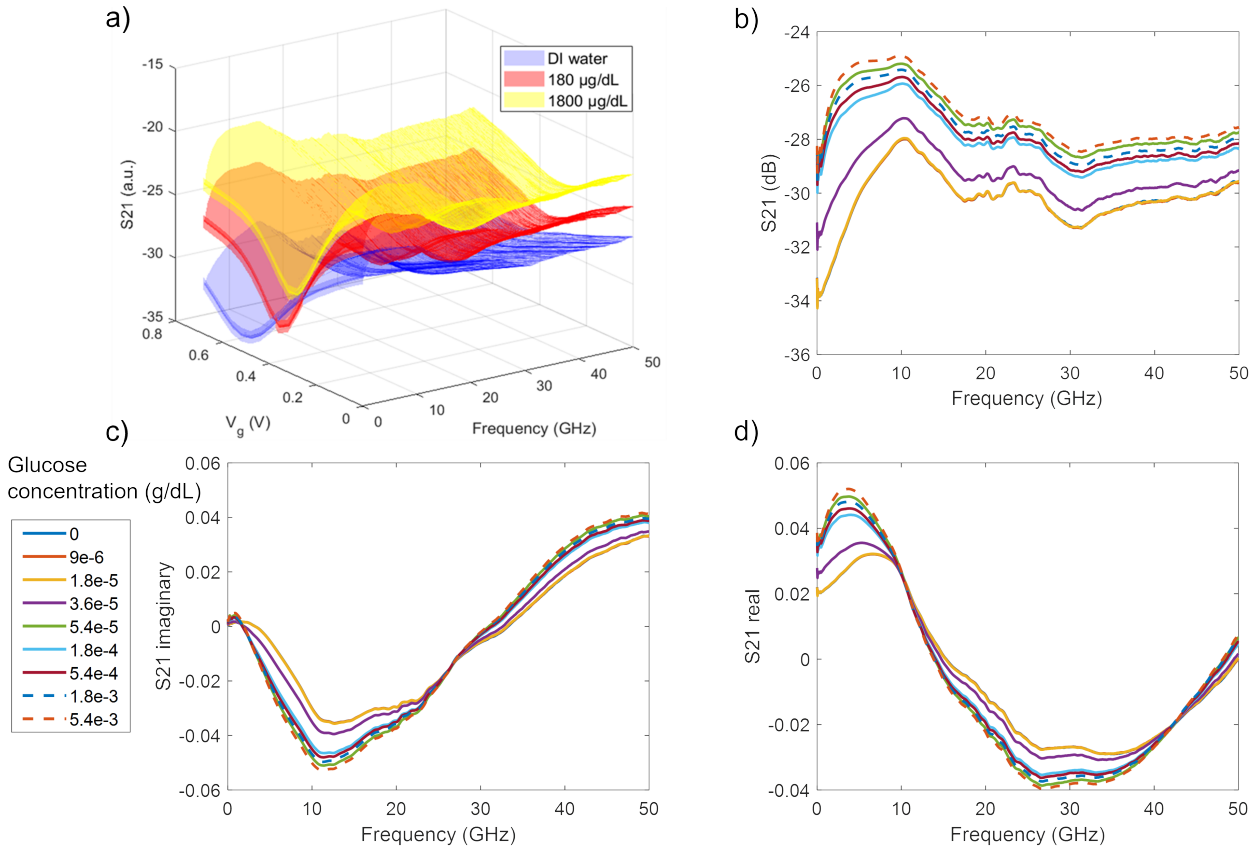

Figure 7: Experimental data visualization. The signal is smoothed by a moving average filter with a window size of 10 to reduce noise without affecting the resonance peak information. The legend of the 'Glucose concentration' is applicable to Figure 7b, 7c, and 7d. a) Comparison of S_{21} amplitude V_g-Frequency surface of three different glucose concentrations. Arbitrary amplitude increments are added to different concentrations to have clearer separations between the surfaces. b) S_{21} amplitude at $V_g = 0.52V$ over the frequency range of 9 different glucose concentrations. c) S_{21} imaginary values at $V_g = 0.52V$ over the frequency range of 9 different glucose concentrations. d) S_{21} real values at $V_g = 0.52V$ over the frequency range of 9 different glucose concentrations.

of each sample after PCA.

The same four parts of S_{21} and S_{11} are used to create Dataset B, but instead of extracting features through PCA, we calculated 5 statistical features from the data. Those features are the Mean, Variance, Peak to RMS difference, Amplitude range, and Standard deviation of the original dataset. Similarly, the final dataset has the dimension of 224×5.

Dataset C makes use of both RF frequency sweep and DC gate voltage sweep. Specifically, for each concentration, each of the four parts of S_{21} and S_{11} at each gate voltage is a sample, and there are 18 different gate voltages from 0.64 V to 0 V, with 1001 features (frequency points) from 50 MHz to 50 GHz. PCA is also utilized to reduce feature dimension, and 6 principal components are obtained with 99% variance explained. Consequently, there are 8×18 samples for each concentration, and the final dataset dimension is 3888×6, with 3888 samples and 6 features for each concentration. By increasing the number of training samples, dataset C is expected to have better represent real experimental cases and can produce a trained model with better generalization performance.

Distinct from the first three datasets, dataset D consists of 2D feature images created from the V_g - Frequency surface of the S_{21} amplitude, instead of the four parts of S_{11} and S_{21}. Specifically, for each concentration, one measurement generates an S_{21} (dB) V_g - Frequency surface, which becomes a feature image of size 18×1001, and the S_{21} (dB) values are mapped to 8-bit grayscale values (0-255). With repeated measurements and three devices with different graphene lengths, 24 feature images are constructed for each concentration, resulting in a total of 648 images.

In summary, datasets A and B only consider the information measured at a specific gate voltage, result-

ing in models that only work with data obtained at that particular gate voltage. Dataset C, on the other hand, includes signals measured at different RF frequencies and DC gate voltages, so the models trained on it can classify data obtained at different gate voltages. Dataset D employs both information from different gate voltages and frequencies in a distinct way from dataset C that the features are in the form of 2D images, so a complete frequency sweep and gate voltage sweep is required to construct the same 2D feature image for each new classification task. A summary of the differences between datasets can be found in Table 1. The composition of predictors may be optimized through physics-based models and careful data analysis instead of adopting PCA and statistical features. Each dataset is split into a training set (80%) and a testing set (20%), and a validation set is created during training based on different criteria for each dataset.

Table 1: The differences between datasets

Dataset	Gate voltage measured (V)	S-parameter components	Feature extraction
A	0.52	real, imaginary parts of S_{21},S_{11}	PCA
B	0.52	real, imaginary parts of S_{21},S_{11}	Calculated
C	0-0.64	real, imaginary parts of S_{21},S_{11}	PCA
D	0-0.64	S_{21} magnitude	Constructed into images

2.7 Glucose Concentration Classification with Machine Learning

To enhance the methodology and leverage the abundant and diverse data from our sensor, we apply several common classification algorithms to the aforementioned datasets to classify solutions with different glucose concentrations. Models are trained with different datasets separately, and their performances are demonstrated and analyzed. The model structures are summarized in the Materials and Methods section.

Table 2 shows the result trained with dataset C. Unlike datasets A and B, which consider data from a specific gate voltage, dataset C encompasses the entire gate voltage range, making it a more challenging yet realistic scenario. Supplementary Table 1 and Supplementary Table 2 provide summaries of the performances of different ML models trained with dataset A and dataset B, respectively. It is observed that the k-nearest neighbor (KNN) has high validation and testing accuracy across all three datasets A, B, and C. Linear Discriminant Analysis (LDA) performs well for datasets A and B but worse for the richer dataset C. The Support Vector Machine (SVM) shows competitive results on dataset C. The Artificial Neural Network (ANN) demonstrates superior results similar to KNN.

To better understand the training process of the neural networks, Figure 8 presents the accuracy and loss curves of training and validation of the ANN. The training accuracy increases with fluctuations and reaches 97% at around 52^{th} epoch (1200^{th} iteration) and 100% at the 135^{th} epoch (3100^{th} iteration); a similar trend is presented in the validation curve, with a final accuracy of 99.5370% and loss equal to 0.0229, which attests to the model's low variance. To mitigate the randomness inherent in neural networks and ensure a robust estimation of the model performance, ten training runs were conducted, resulting in an average validation accuracy of 99.6065% with a standard deviation of 0.4233%. 432 new samples are used for testing, with a testing accuracy of 100%. The fluctuations in the figures show that using a lower learning rate or a bigger batch size may be beneficial, but the training time will increase accordingly.

Table 2: ML model performance on dataset C

Classification Algorithms	Validation Accuracy (%)	Testing Accuracy (%)
KNN	97.9	100
LDA	93.4	91.9
Tree	82.2	82.9
SVM	95.5	94.4
ANN	99.6	100

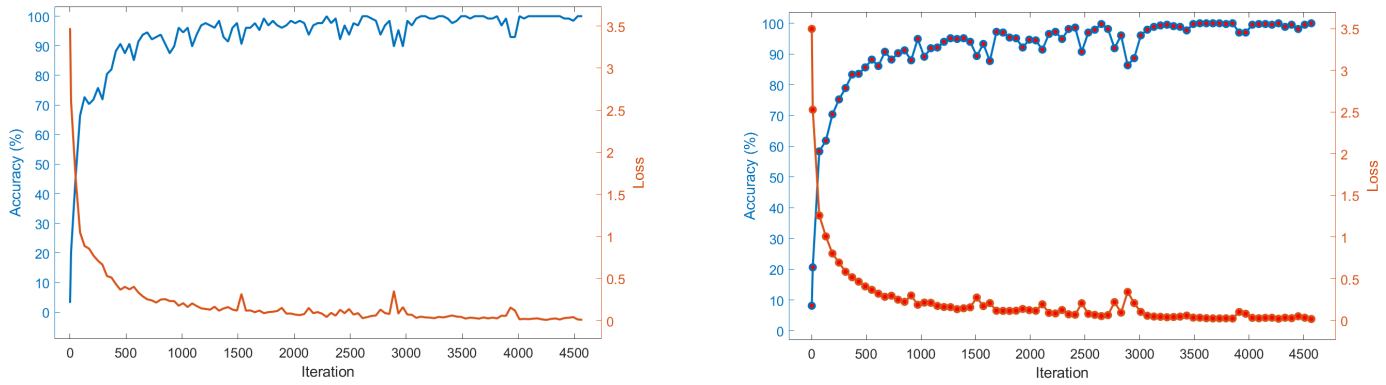

(a) Training curves. (b) Validation curves.

Figure 8: Accuracy and Loss curves of Training and Validation of ANN.

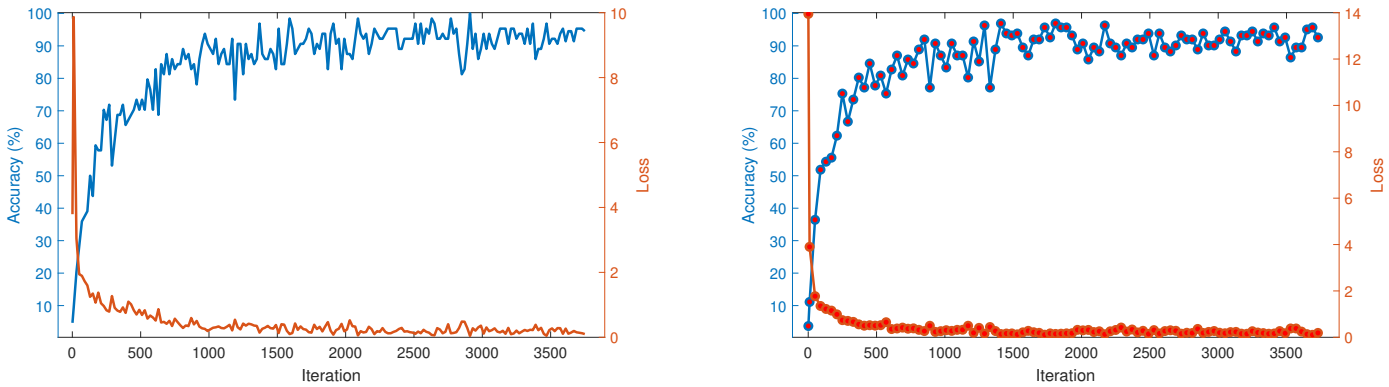

(a) Training curves. (b) Validation curves.

Figure 9: Accuracy and Loss curves of Training and Validation of CNN.

The convolution kernels in the CNN extract new feature maps from the feature images for the classification task. The result curves of the three-layer CNN trained with dataset D have similar trends to those of ANN trained with dataset C, as shown in Figure 9. After $\sim$ 250 epochs (1500 iterations), the training accuracy converges to around 97%, and the final validation accuracy and loss are 95.68% and 0.1849, respectively. The other three sets of new data (81 samples) are used for testing, and the testing accuracy is 95.06%, which is slightly worse than the result of the ANN trained with dataset C.

2.8 Machine Learning Result Discussion

For the classification problem studied in this paper, the employed ML models are capable of classifying glucose concentrations with very small variations (down to $9\,\mu g\,dL^{-1}$) based on different datasets consisting of S-parameters measured with different DC gate voltages or at different RF frequencies. Specifically, the considered glucose concentrations in this paper are much lower than those in previously reported [51] on a similar glucose classification task. We can see models trained with datasets A and B have very high accuracy; however, only the testing data obtained at a determined gate voltage is considered, and the models lack robustness against the testing data with the shift of different gate voltages. KNN, SVM, and ANN trained with dataset C, which considers both the RF frequency and DC gate voltage sweeps, achieved good classification results, indicating good robustness, and ANN yielded the highest validation accuracy. The CNN model trained with 'feature images' also performs well on the classification task. The small disadvantage in accuracy may be due to a lack of enough samples and S_{11} information for each concentration. Also, the loss may continue to decline with more training epochs. On the basis of aqueous glucose, the attempt of CNN demonstrates the potential of leveraging the 2D S-

parameter feature images and the power of convolutional layers for complex chemical or biologic analyte classification in multi-sensing applications using the approaches presented in this work.
Also, according to the confusion matrices (Supplementary Figure7 and Figure8) of different models, the results are highly accurate at glucose concentrations larger than $0.5\,\mathrm{g\,dL^{-1}}$ but struggle with lower concentrations. ANN and Linear SVM perform well at very small concentrations but worse at around $0.05\,\mathrm{g\,dL^{-1}}$ and $0.4\,\mathrm{g\,dL^{-1}}$. This suggests that further work should focus on concentrations below $0.5\,\mathrm{g\,dL^{-1}}$, and the performance of different models can vary in practice according to the feature compositions and the concentration range of interest.
Note that due to the limited amount of training and testing datasets, the generalization and stability of the current models to other sensing tasks require further verification, especially for the ANN and CNN models that rely heavily on a sufficient database. However, the presented results demonstrate the great potential of ML to achieve outstanding performance in detecting molecules with the proposed device.
One advantage of the data-driven approach is that, except for common data preprocessing steps, the measured data do not require precise and complicated calibrations before being fed to ML models. This can lead to faster and more robust solutions by mitigating the impact of experimental errors, approximations, and physical model assumptions. Moreover, the short training time of ML models and the advantage of analyzing new data and generating predictions instantaneously using trained models make ML methods well-suited for real-time applications.
In addition to classification, concentration prediction of aqueous glucose solutions was also attempted with ML. However, because we only looked at a few discrete glucose concentrations, classification is a more reasonable goal to pursue. The large R-squared values and the small root-mean-square errors (RMSE) of the prediction results may suffer over-fitting. Nevertheless, established on the result of the ML model trained with simulation data, the feasibility of using the proposed approaches for regression is validated and worth further research. More discussions on regression are presented in Supplementary Information.

3 Conclusion

We presented a novel approach for glucose sensing based on graphene microwave waveguides interfaced with microfluidic channels. Our sensors do not require functionalization and combine the functionalities of ChemFETs and microwave sensors in a single device, resulting in a sensitivity of 7.30 dB/(mg/L) at concentration down to $9\,\mathrm{\mu g\,dL^{-1}}$. The maximum sensitivity is achieved at 2.13 GHz, making our sensor easily compatible with conventional electronics components and circuitry used in wireless communication technology. Our devices produce information-rich, multidimensional datasets in the form of (complex) scattering parameters which depend on the glucose concentration and electrochemical gate voltage. In order to capture such rich datasets as a whole, we analyzed the data using different ML models, achieving 100% classification accuracy on the testing set. We anticipate that our sensing and data analysis approaches can be extended to more complex substances or mixtures with multiple analytes, where the data is richer and exhibits higher dimensions and non-linearities. Moreover, we note that the sensor and the measuring setup could be scaled down to a single chip, as already demonstrated in systems consisting of multisection directional couplers and VNAs integrated on the same chip [66] or by combining our sensors with commercially available VNA chips.

4 Experimental Section

Graphene Growth and transfer.:
Graphene was grown on 25 µm thick Cu foil (Alfar Aesar) using a cold-walled CVD reactor (AIXTRON BM PRO 4) following the method described in Ref. [67]. PMMA 495 (4% concentration in anisole) was spincoated on the graphene on the copper foil. The copper foil was floated on the surface of an ammonium persulfate (APS) solution (1g per 150mL DI water), PMMA side up. Once the copper is etched, the PMMA-graphene film was deposited onto DI water to remove any APS residue. The film was then

transferred onto a cleaned undoped Si wafer covered in 285nm-thick, thermally-grown SiO_2. Once dry, the sample on the Si wafer was submerged in acetone for 8 hours, transferred to a clean acetone bath for 8 hours and then into an isopropyl alcohol (IPA) bath for 10 minutes to remove the PMMA. The graphene on the wafer was then annealed in air at 150°C for 5 minutes.

Device fabrication.:
After transfer, the chip was spin-coated with AZ5214E photoresist and pre-baked at 100 °C for 1 minute before direct-write laser lithography (Microtech Srl LW-405B). The exposed areas were etched using 10 W oxygen plasma for 1 minute, after which the sample was spin-coated again with AZ5214E for lithography of the metal layer. Before metal deposition, the graphene was pretreated using a weak argon plasma (0.5 W for 30 s) through the same mask to reduce contact resistance. We deposited 5 nm Cr and 100 nm Au, using Cr as the adhesion layer. To fabricate the microfluidic channel, a negative mold was made using SU8-2100 epoxy resin photoresist and 365 nm direct-write laser lithography. PDMS (Sylgard 184) was mixed according to manufacturer specification and cast, then held under vacuum for 1hr to eliminate any air bubbles, after which the sample was cured at 100 °C for 6 hours. The PDMS layer was extracted from the mold and trimmed, and feedholes were introduced. The PDMS channel was aligned with the structures on the Si wafer, and microfluidic feedlines were attached and sealed using liquid PDMS. To achieve stronger adhesion and cure the PDMS seals, the produced sample was held in an oven at 80 °C overnight.

Electrical Measurements.:
DC and RF Electrical measurements were performed using a Cascade Summit 1200 semi-automatic probe station equipped with DC and RF (GSG) probes. 50MHz-50GHz bias networks (Keysight) were used to apply both DC and RF *via* the same probe. DC measurements were performed by an Agilent B1500A parameter analyzer, and RF measurements were acquired by an Agilent PNA-X 5245 VNA. The system was calibrated to bring the measurement plane to the probe tips using the Cascade Microtech 101-190C standard impedance substrate (ISS) using the mTRL technique and WinCal calibration routines, which consisted of repeated measurements on 1 ps, 3 ps and 7 ps 50 Ω THRU delay lines, i.e. lengths of 220 µm, 450 µm and 900 µm on the alumina substrate [68, 69]. Glucose solutions were introduced by an ElveFlow OB1 Mk3 microfluidic setup. To ensure repeatability and optimize the large-scale data collection, we developed a software routine that performed the measurements automatically, moving and landing the probes through the array of devices and synchronizing the DC and RF measurement equipment.

Supporting Information
Supporting Information is available from the Wiley Online Library or from the author. Supporting information include:

1. Finite element electromagnetic simulations
2. Experimental and simulation comparison between metallic and graphene waveguides
3. Machine learning models and additional results

Acknowledgements
We acknowledge funding from EPSRC grant EP/L016087/1.

Author Contributions
P.G. and T.X. contributed equally.

References

[1] F. Kremer, A. Schönhals, *Broadband Dielectric Spectroscopy*, Springer Science & Business Media, **2002**.

[2] K. Grenier, D. Dubuc, T. Chen, F. Artis, T. Chretiennot, M. Poupot, J.-J. Fournié, *IEEE Transactions on Microwave Theory and Techniques* **2013**, *61*, 5 2023.

[3] M. Cifra, J. Prusa, D. Havelka, O. Krivosudsky, *IEEE Journal of Electromagnetics, RF and Microwaves in Medicine and Biology* **2018**, *3*, 2 97.

[4] V. Raicu, Y. Feldman, *Dielectric Relaxation in Biological Systems: Physical Principles, Methods, and Applications*, Oxford University Press, USA, **2015**.

[5] K. C. Kao, *Dielectric Phenomena in Solids*, Elsevier, **2004**.

[6] G. Guarin, M. Hofmann, J. Nehring, R. Weigel, G. Fischer, D. Kissinger, *IEEE Microwave Magazine* **2015**, *16*, 4 71.

[7] M. Hofmann, T. Fersch, R. Weigel, G. Fischer, D. Kissinger, In *2011 IEEE International Symposium on Medical Measurements and Applications*. **2011** 39–42.

[8] G. R. Pecorella, G. Verderame, A. Lombardo, P. Livreri, In *2022 IEEE International Instrumentation and Measurement Technology Conference (I2MTC)*. **2022** 1–6.

[9] H.-W. Wu, *IEEE Transactions on Microwave Theory and Techniques* **2016**, *64*, 3 982.

[10] S. Seo, T. Stintzing, I. Block, D. Pavlidis, M. Rieke, P. G. Layer, In *2008 IEEE MTT-S International Microwave Symposium Digest*. **2008** 915–918.

[11] F. Artis, T. Chen, T. Chretiennot, J.-J. Fournie, M. Poupot, D. Dubuc, K. Grenier, *IEEE Microwave Magazine* **2015**, *16*, 4 87.

[12] G. Guariti, M. Hofmann, R. Weigel, G. Fischer, D. Kissinger, In *2013 IEEE MTT-S International Microwave Symposium Digest (MTT)*. **2013** 1–4.

[13] O. Krivosudskỳ, D. Havelka, D. E. Chafai, M. Cifra, *Sensors and Actuators B: Chemical* **2021**, *328* 129068.

[14] T. Chretiennot, D. Dubuc, K. Grenier, *Sensors* **2016**, *16*, 10 1733, number: 10 Publisher: Multidisciplinary Digital Publishing Institute.

[15] P. Gubeljak, L. Pedrazzetti, O. J. Burton, L. Magagnin, S. Hofmann, G. G. Malliaras, A. Lombardo, In *2022 IEEE International Symposium on Medical Measurements and Applications (MeMeA)*. **2022** 1–6.

[16] P. Gubeljak, T. H. Xu, L. Pedrazzetti, O. J. Burton, L. Magagnin, S. Hofmann, G. G. Malliaras, A. Lombardo, *Nanoscale* **2023**, *15*, 37 15304, s6qw2 Times Cited:1 Cited References Count:57.

[17] K. S. Novoselov, A. K. Geim, S. V. Morozov, D.-e. Jiang, Y. Zhang, S. V. Dubonos, I. V. Grigorieva, A. A. Firsov, *science* **2004**, *306*, 5696 666.

[18] F. Schedin, A. K. Geim, S. V. Morozov, E. W. Hill, P. Blake, M. I. Katsnelson, K. S. Novoselov, *Nature Materials* **2007**, *6*, 9 652.

[19] I. Prattis, E. Hui, P. Gubeljak, G. S. K. Schierle, A. Lombardo, L. G. Occhipinti, *Trends in Biotechnology* **2021**, *39*, 10 1065.

[20] Y. Liu, F. Meng, Y. Zhou, S. M. Mugo, Q. Zhang, *Advanced Materials Technologies* **2019**, *4*, 11 1900540.

[21] M. Allen, A. Bessonov, T. Ryhänen, *SID Symposium Digest of Technical Papers* **2021**, *52*, 1 987.

[22] *Nature Materials* **2021**, *20*, 5 573.

[23] M. Zhou, Y. Zhai, S. Dong, *Analytical Chemistry* **2009**, *81*, 14 5603–5613.

[24] F. Chen, Q. Qing, J. Xia, J. Li, N. Tao, *Journal of the American Chemical Society* **2009**, *131*, 29 9908–9909.

[25] H. Li, H. Sun, J. Ding, T. Wu, S. Cai, C. Wang, R. Yang, *Microchimica Acta* **2022**, *189*, 7 261.

[26] F. Li, B. Zhang, B. Yan, Q. Chen, X. Wang, K. Zhang, H. Pei, Q. Wu, D. Chen, J. Tu, *AIP Advances* **2022**, *12*, 6 065208.

[27] A. Bazan-Aguilar, M. Ponce-Vargas, C. L. Caycho, A. L. Rosa-Toro, A. M. Baena-Moncada, *ACS Omega* **2020**, *5*, 50 32149.

[28] J. G. Brandenburg, A. Zen, M. Fitzner, B. Ramberger, G. Kresse, T. Tsatsoulis, A. Grüneis, A. Michaelides, D. Alfè, *The Journal of Physical Chemistry Letters* **2019**, *10*, 3 358.

[29] S. Awan, A. Lombardo, A. Colli, G. Privitera, T. Kulmala, J. Kivioja, M. Koshino, A. Ferrari, *2D Materials* **2016**, *3*, 1 015010.

[30] J. Horng, C.-F. Chen, B. Geng, C. Girit, Y. Zhang, Z. Hao, H. A. Bechtel, M. Martin, A. Zettl, M. F. Crommie, Y. R. Shen, F. Wang, *Phys. Rev. B* **2011**, *83* 165113.

[31] I.-T. Lin, J.-M. Liu, *IEEE Journal of Selected Topics in Quantum Electronics* **2014**, *20*, 1 122.

[32] Y.-W. Tan, Y. Zhang, K. Bolotin, Y. Zhao, S. Adam, E. H. Hwang, S. Das Sarma, H. L. Stormer, P. Kim, *Phys. Rev. Lett.* **2007**, *99* 246803.

[33] M. Mittendorff, F. Wendler, E. Malic, A. Knorr, M. Orlita, M. Potemski, C. Berger, W. A. de Heer, H. Schneider, M. Helm, S. Winnerl, *Nature Physics* **2014**, *11*, 1 75.

[34] J. Roelvink, S. Trabelsi, S. O. Nelson, *IEEE Transactions on Instrumentation and Measurement* **2013**, *62*, 11 2974.

[35] J. R. Baker-Jarvis, M. D. Janezic, B. F. Riddle, R. T. Johnk, C. L. Holloway, R. G. Geyer, C. A. Grosvenor **2005**.

[36] M. Degerstrom, B. K. Gilbert, E. Daniel, In *2008 IEEE-EPEP Electrical Performance of Electronic Packaging*. IEEE, **2008** 77–80.

[37] W. R. Eisenstadt, Y. Eo, *IEEE transactions on components, hybrids, and manufacturing technology* **1992**, *15*, 4 483.

[38] M. Gusev, L. Poposka, G. Spasevski, M. Kostoska, B. Koteska, M. Simjanoska, N. Ackovska, A. Stojmenski, J. Tasic, J. Trontelj, *Journal of Sensors* **2020**, *2020*.

[39] F. Cui, Y. Yue, Y. Zhang, Z. Zhang, H. S. Zhou, *ACS sensors* **2020**, *5*, 11 3346.

[40] T. Kim, S. Moon, K. Xu, *Nature communications* **2019**, *10*, 1 1.

[41] Y. Li, A. Mahjoubfar, C. L. Chen, K. R. Niazi, L. Pei, B. Jalali, *Scientific reports* **2019**, *9*, 1 1.

[42] M. Erzina, A. Trelin, O. Guselnikova, B. Dvorankova, K. Strnadova, A. Perminova, P. Ulbrich, D. Mares, V. Jerabek, R. Elashnikov, et al., *Sensors and Actuators B: Chemical* **2020**, *308* 127660.

[43] J. Dai, Z. Ji, Y. Du, S. Chen, *Technology and Health Care* **2018**, *26*, S1 229.

[44] L. Harrsion, M. Ravan, D. Tandel, K. Zhang, T. Patel, R. K Amineh, *Electronics* **2020**, *9*, 2 288.

[45] B. Jamali, D. Ramalingam, A. Babakhani, *IEEE Sensors Letters* **2020**, *4*, 7 1.

[46] Q. Chen, K.-M. Huang, X. Yang, M. Luo, H. Zhu, *Progress In Electromagnetics Research* **2011**, *116* 347.

[47] T. Hayasaka, A. Lin, V. C. Copa, L. P. Lopez Jr, R. A. Loberternos, L. I. M. Ballesteros, Y. Kubota, Y. Liu, A. A. Salvador, L. Lin, *Microsystems & nanoengineering* **2020**, *6*, 1 50.

[48] C. G. Juan, E. Bronchalo, B. Potelon, C. Quendo, E. Ávila-Navarro, J. M. Sabater-Navarro, *IEEE Transactions on Instrumentation and Measurement* **2018**, *68*, 7 2621.

[49] C. G. Juan, B. Potelon, C. Quendo, E. Bronchalo, J. M. Sabater-Navarro, In *2019 49th European Microwave Conference (EuMC)*. IEEE, **2019** 662–665.

[50] V. Turgul, I. Kale, *Sensors and Actuators A: Physical* **2018**, *277* 65.

[51] M. S. Hossain, Y. Zhou, In *2020 IEEE International Symposium on Antennas and Propagation and North American Radio Science Meeting*. **2020** 1613–1614.

[52] C. G. Juan, E. Bronchalo, B. Potelon, C. Quendo, J. M. Sabater-Navarro, *Sensors* **2019**, *19*, 17 3779.

[53] M. S. Hossain, Y. Zhou, In *2020 IEEE International Symposium on Antennas and Propagation and North American Radio Science Meeting*. **2020** 1613–1614, ISSN: 1947-1491.

[54] S. M. Bamatraf, M. A. Aldhaeebi, O. M. Ramahi, *Progress in Electromagnetics Research Letters* **2022**, *102*.

[55] N. Kazemi, M. Abdolrazzaghi, P. E. Light, P. Musilek, *Biosensors and Bioelectronics* **2023**, *241* 115668.

[56] FormFactor, *Infinity Probe® Mechanical Layout Rules*, **2022**.

[57] S. Xu, J. Zhan, B. Man, S. Jiang, W. Yue, S. Gao, C. Guo, H. Liu, Z. Li, J. Wang, et al., *Nature communications* **2017**, *8*, 1 14902.

[58] M. Güemes, S. A. Rahman, K. Hussain, *Archives of Disease in Childhood* **2016**, *101*, 6 569–574.

[59] M. Zhang, C. Liao, C. H. Mak, P. You, C. L. Mak, F. Yan, *Scientific reports* **2015**, *5*, 1 8311.

[60] Y. Zhu, Y. Hao, E. A. Adogla, J. Yan, D. Li, K. Xu, Q. Wang, J. Hone, Q. Lin, *Nanoscale* **2016**, *8*, 11 5815.

[61] C. G. Juan, E. Bronchalo, G. Torregrosa, E. Ávila, N. García, J. M. Sabater-Navarro, *Biomedical Signal Processing and Control* **2017**, *31* 139.

[62] D. Sankhala, A. U. Sardesai, M. Pali, K.-C. Lin, B. Jagannath, S. Muthukumar, S. Prasad, *Scientific Reports* **2022**, *12*, 1 2442.

[63] C. G. Juan, B. Potelon, C. Quendo, E. Bronchalo, *Applied Sciences* **2021**, *11*, 15.

[64] S. Y. Huang, Omkar, Y. Yoshida, A. J. G. Inda, C. X. Xavier, W. C. Mu, Y. S. Meng, W. Yu, *IEEE Sensors Journal* **2019**, *19*, 2 535.

[65] M. A. Zidane, A. Rouane, C. Hamouda, H. Amar, *Sensors and Actuators A: Physical* **2021**, *321* 112601.

[66] J. Nehring, M. Schütz, M. Dietz, I. Nasr, K. Aufinger, R. Weigel, D. Kissinger, *IEEE Transactions on Microwave Theory and Techniques* **2017**, *65*, 1 229.

[67] O. J. Burton, V. Babenko, V.-P. Veigang-Radulescu, B. Brennan, A. J. Pollard, S. Hofmann, *The Journal of Physical Chemistry C* **2019**, *123*, 26 16257.

[68] Cascade Microtech®, *Impedance Standard Substrate*, **2007**, URL `https://www.formfactor.com/product/probes/calibration-tools-probes/impedance-standard-substrates/`, 101-971 rev E.

[69] FormFactor, Inc., *Consistent Parameter Extraction for Advanced RF Devices*, **2020**.

Table of Contents

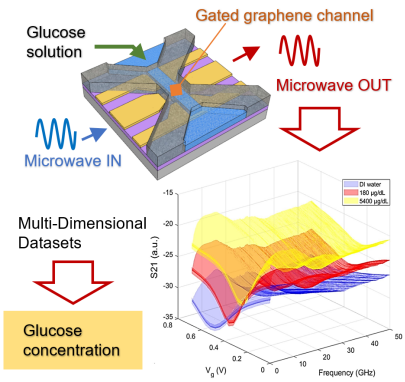

This paper demonstrates a novel approach for glucose detection based on graphene microwave waveguides. By combining the frequency-dependent interaction with microwaves and changes in graphene conductivity due to physisorbed molecules, the sensor achieves a sensitivity of 7.30 dB/(mg/L) and produces multidimensional datasets. Different machine learning methods are applied, achieving classification accuracy of 100% with variations as low as 0.09 mg/L.